

# Mechanisms of X-ray and gamma-ray emissions in lightning and spark discharges

N.I. Petrov

*Scientific and Technological Centre of Unique Instrumentation of the Russian Academy of Sciences,  
15 Butlerova str., Moscow, 117342 Russia*

*E-mail: [petrovni@mail.ru](mailto:petrovni@mail.ru)*

**Abstract:** X-ray and  $\gamma$ -ray emissions observed in lightning and long sparks are usually connected with the bremsstrahlung of high-energy runaway electrons. Here, an alternative physical mechanism for producing X-ray and gamma-ray emissions caused by the polarization current and associated electromagnetic field moving with relativistic velocity along a curved discharge channel has been proposed. It is pointed out that lightning and spark discharges should also produce a coherent radio-frequency radiation. The influence of the conductivity and the radius of the lightning channel on the propagation velocity of electromagnetic waves, taking into account the absorption, have been investigated. The existence of fast electromagnetic surface waves propagating along the lightning discharge channel at a speed close to the speed of light in vacuum is shown. The possibility of the production of microwave, X-ray and gamma-ray emissions by a polarization current pulse moving along a curved path via synchrotron radiation mechanism during the lightning leader steps formation and the very beginning of the return stroke stage is pointed out. The existence of long tails in the power spectrum is shown, which explains observations of photon energies in the range of 10-100 MeV in the TGF, as well as measured power spectrum of laboratory spark discharge.

## 1. Introduction

Lightning discharges are the most common source of powerful electromagnetic fields of natural origin. It is well known that lightning radiation covers almost the entire wavelength range, from a few hertz to ultraviolet. It was suggested in [1], that the strong electric fields in thunderclouds could trigger nuclear reactions. Recently, the first observational evidence of photonuclear reactions triggered by lightning discharge was reported [2]. In recent decades, a phenomenon of terrestrial gamma-ray flashes (TGF) generated during thunderstorms was discovered [3]. It was established that both thunderclouds and lightning regularly emit X-rays and gamma rays. Gamma-ray flashes from natural [4, 5] and rocket-triggered [6] lightning, as well as from laboratory spark discharge were observed [7]. It is generally assumed that the TGF photons are produced via the bremsstrahlung of runaway electrons accelerated by high electric fields in the atmosphere [8]. Currently, two models of electron acceleration and multiplication based on the relativistic runaway electron avalanche (RREA) mechanism [9, 10] and the lightning leader model [11, 12] have been proposed. These models explain the multiplication of energetic electrons and the subsequent production of bremsstrahlung photons.

However, some basic properties, such as the radiation spectrum (in the region above 10 MeV), the cut-off energy, and the polarization and beaming characteristics of the radiation still need to be explained. It is also important to clarify the relationship between the parameters of TGF and the characteristics of lightning discharge channel.

It follows from ground-based observations that TGFs are associated with cloud-to-ground discharges of negative polarity. Measurements show that X-rays from natural lightning and intense bursts of gamma-ray radiation with energies up to 10 MeV are correlated with negative leader stepping [9, 10]. The detection of TGF emission with photon energies in the 10-100 MeV range was reported in [13]. It was shown that the detected power-law radiation in the range from 10 to 100 MeV is difficult to explain using RREA models [9-12].

Recent observations have shown that gamma radiation correlates with radio-frequency radiation and is generated at the last stage of lightning leader channel development prior to the lightning return stroke [14]. The bursts of 30-80 MHz radiation because of leader stepping were observed in [15]. It was shown in [16] that TGF is produced in the initial stage of a lightning flash just before the initiation of the current pulse. Observations of TGFs which occur at the onset of UV and optical emissions also point to the importance of lightning leaders [16-19].

In this paper, the mechanism of production of X-ray and  $\gamma$ -ray emissions by polarization current and associated surface electromagnetic wave propagating along the ionized lightning channel with relativistic velocities is proposed. The possibility of the production of X-ray and gamma-ray emissions from a polarization current pulse moving along a curved path during the lightning leader steps formation and last stage of lightning leader channel (final jump phase - the very beginning of the first and subsequent return stroke stages) is pointed out.

## 2. Physical model

The streamer-leader process underlies the development of lightning and spark discharges in the atmosphere [10]. The embedded charges distributed within the leader channel are neutralized during the leader step processes or during the lightning return stroke. It is established that the front of the neutralization process moves along the channel at a speed of the order of the speed of light [10]. High frequency electromagnetic wave modes are excited in the lightning discharge channels during the leader step processes or during grounding. It is well known that the surface electromagnetic waves can propagate along the conducting wire [20]. Here, we show that fast surface electromagnetic waves with the velocities close to the speed of light in vacuum can propagate along the ionized channel of the lightning leader over a limited distance.

The electromagnetic field behaviour in a lightning channel is described by the dispersion equation which is followed from the Maxwell equations. For the cylindrical structure of plasma channel the eigenmodes may be determined from the Helmholtz equations for the longitudinal field component  $E_z$ :

$$\begin{aligned} \left[ \nabla_{\perp}^2 + (k_0^2 \varepsilon_p - \beta^2) \right] E_z &= 0, \quad 0 < r < r_0 \\ \left[ \nabla_{\perp}^2 + (k_0^2 - \beta^2) \right] E_z &= 0, \quad r > r_0, \end{aligned} \quad (1)$$

where  $\nabla_{\perp}^2 = \frac{1}{r} \frac{\partial}{\partial r} \left( r \frac{\partial}{\partial r} \right) + \frac{1}{r^2} \frac{\partial^2}{\partial \varphi^2}$ ,  $k_0 = \omega/c$  is the wavenumber in free space,  $\beta$  is the longitudinal component of the wavenumber,  $r_0$  is the channel radius,  $\varepsilon_p = \varepsilon' + i \frac{\sigma}{\omega \varepsilon_0}$  is the complex dielectric constant, where  $\sigma = \frac{1}{R_l \pi r_0^2}$  is the electric conductivity,  $R_l$  is the resistance per unit length, and  $\varepsilon_0$  is the dielectric constant of free space.

Solutions of the equations (1) are the Bessel functions:

$$E_z = \begin{cases} A_1 I_0(\eta r), & r \leq r_0 \\ A_2 K_0(\eta_0 r), & r \geq r_0 \end{cases}, \quad (2)$$

where  $A_1$  and  $A_2$  are the amplitude coefficients,  $I_0$  and  $K_0$  are the modified Bessel functions of the first and second kind,  $\eta^2 = (\omega^2/c^2) \varepsilon_p - \beta^2$ ,  $\eta_0^2 = (\omega^2/c^2) - \beta^2$ .

The wave fields (2) are localized near the plasma-air boundary, so the wave is a surface wave propagating along the channel boundary.

Dispersion equation for the surface electromagnetic waves is followed from the boundary condition of continuity of the tangential components of the field at  $r = r_0$ :

$$\frac{\varepsilon_p I_0'(\eta a)}{\eta a I_0(\eta a)} = \frac{1}{\eta_0 a} \frac{K_0'(\eta_0 a)}{K_0(\eta_0 a)}, \quad (3)$$

where  $I_0'$  and  $K_0'$  are the derivatives of the Bessel functions.

Phase and group velocities of the surface wave can be determined from the dispersion equation (3).

The wavevector  $\beta = \beta' + i\beta''$  is a complex value. The real part  $\beta'$  defines the phase velocity  $V_{ph} = \omega/\beta'$  of the wave, and the group velocity is determined by  $V_g = d\omega/d\beta'$ . The imaginary part  $\beta''$  defines the attenuation length  $z_0 = 1/\beta''$  of the surface wave propagating along the discharge channel.

In Fig.1 the velocity and the attenuation length of the surface wave as a function of the frequency, conductivity and radius of the discharge channel are presented.

It follows from the simulation that the velocity increases with the frequency. The propagation distance of the surface wave decreases when the frequency increases (Figs. 1a, b). Only the components of the current pulse with frequencies of the order of MHz and lower reach high altitudes of the order of a kilometer or more. For a given frequency the velocity is higher for the higher electric conductivity of a channel and the propagation distance increases with the conductivity (Figs. 1c, d). The velocity and propagation distance of the surface waves increase with the radius of a discharge channel (Figs. 1e, f). Thus, the speed of surface waves increases with frequency, as well

as with the conductivity and radius of a discharge channel (Fig. 1). These waves are attenuated during propagation along the channel because of the skin effect. Dissipation increases with frequency because of the skin effect. The propagation distance of surface waves decreases with frequency because of dissipation (Fig.1b). However, this distance increases with the conductivity and radius of a discharge channel (Fig. 1d, e). It follows that ultra-relativistic velocities of the order of the speed of light in vacuum are achieved for high-frequency waves at the conductivities and radii of the discharge channel characteristic of lightning.

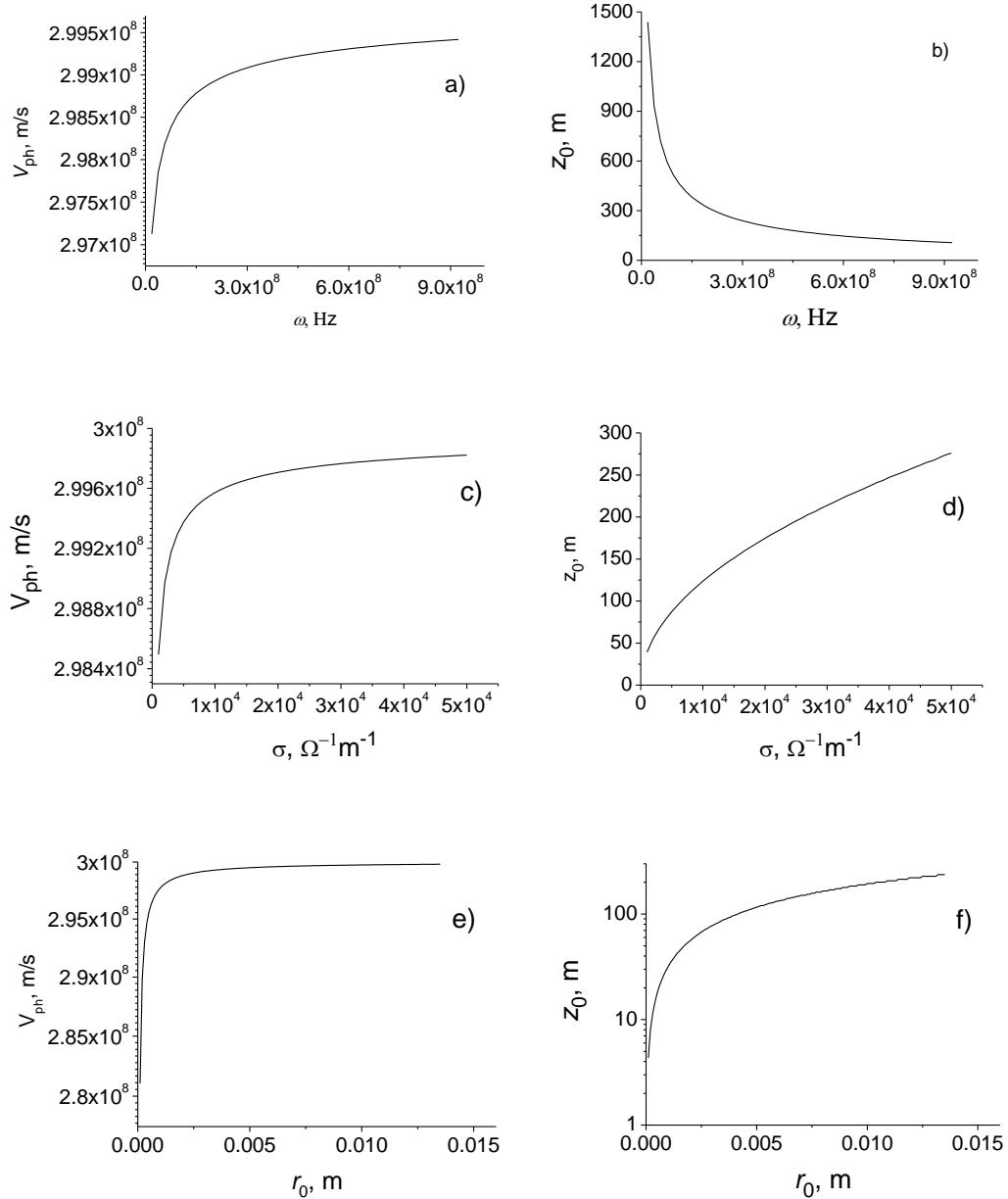


Fig. 1. Velocity and attenuation length as function of frequency (a, b), conductivity (c, d) and channel radius (e, f). (a, b) -  $\sigma = 10^4 \Omega^{-1}m^{-1}$ ,  $r_0 = 0.01$  m; (c, d) -  $\omega = 2\pi f = 10^9$  Hz,  $r_0 = 0.01$  m; (e, f) -  $\omega = 2\pi f = 3 \cdot 10^{10}$  Hz,  $\sigma = 10^5 \Omega^{-1}m^{-1}$ .

The velocity of surface waves increases with frequency, as well as with the conductivity and radius of the discharge channel (Fig. 1). These waves are attenuated when propagating through the channel due to the skin effect. The dissipation increases with frequency due to a decrease in the thickness of the skin layer:  $\delta = \left( \frac{2\varepsilon_0 c^2}{\omega\sigma} \right)^{1/2}$ . The propagation distance of surface waves decreases with the

increase of the frequency due to dissipation (Fig. 1). However, this distance increases with increasing conductivity and the radius of the discharge channel.

It follows from the simulation that phase velocities of the order of the speed of light in vacuum are achieved for the channel conductivity and the radii characteristic of lightning.

In Fig. 2a the phase and group velocities are presented as a function of surface wave frequency. It is seen that  $V_g > V_{ph}$ . In Fig. 2b the dependence of the attenuation length on the frequency is shown.

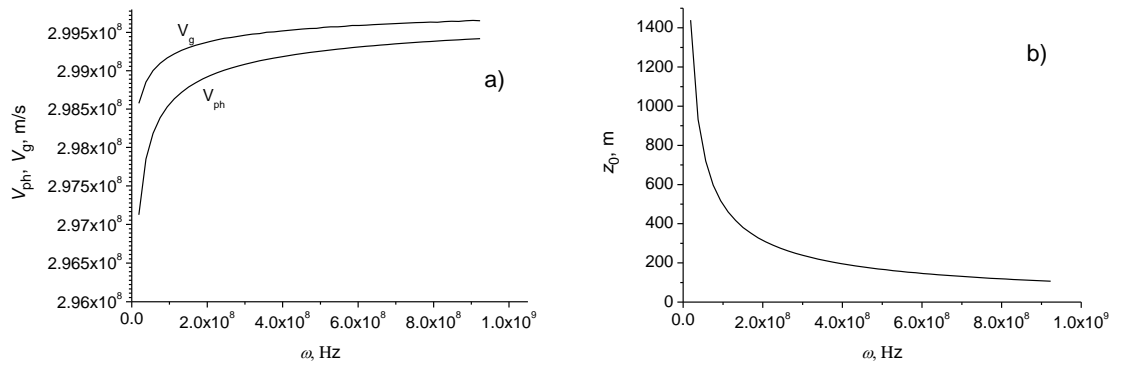


Fig. 2. Phase and group velocity (a), and attenuation length (b) as function of frequency.

The group velocity  $V_g = d\omega/d\beta'$  can be expressed as  $V_g = V_{ph} - \lambda(dV_{ph}/d\lambda)$ . Since  $dV_{ph}/d\lambda < 0$ , then  $V_g > V_{ph}$ . This indicates that abnormal dispersion occurs at these frequencies. The group velocity determines the velocity of propagation of the amplitude of the envelope of a wave packet formed as a result of interference (beats) of waves with close frequencies. Note that in a non-dispersive medium, the group velocity of the guided modes is less than the phase velocity [21].

At present, there is a sufficient amount of measured data on the parameters of lightning and spark discharge in the laboratory. In [22] the diameter of the lightning stroke was measured by allowing lightning discharges to pass through fiberglass screen. The diameters of the holes produced in fiberglass screen were varied from 2 mm to 3.5 cm. It was shown in [23] that the channel diameter determined from the 224 images obtained with a high-speed framing camera has a mean value of 6.5 cm.

Note that the surface plasmon wave causes an additional ionization resulting in generation of the higher plasma density. It was shown that the electron density of the lightning stepped leader is of the order of  $10^{24} \text{ m}^{-3}$  [24]. The measurements show that the resistances per unit length of the lightning channel are of the order of  $10^{-2}$ – $10^{-1} \Omega/\text{m}$  and the internal electric field strengths are of the order of  $10^3 \text{ V/m}$  [25]. For the resistance per unit length  $R_l = 10^{-2} \Omega/\text{m}$  and the channel radius  $r_0 = 6 \text{ mm}$  we

have the conductivity  $\sigma = \frac{1}{R_l \pi r_0^2} \approx \frac{1}{10^{-2} \cdot 10^{-4}} \sim 10^6 \Omega^{-1} \text{m}^{-1}$ . The same order of conductivity follows from the Drude model for the electron density of the lightning leader  $n = 10^{24} \text{m}^{-3}$ . In the laboratory spark discharges the conductivity has lower values:  $R_l \sim 10 \Omega/\text{m}$  [26].

The calculations show that a fast surface electromagnetic wave of high frequency propagates on the surface of the plasma channel at a speed close to the speed of light in vacuum. Surface plasmon waves, which are the combination of the polarization density (electric dipoles) wave and the electromagnetic wave, propagate along the lightning leader channel. These high frequency guided waves are generated during the lightning leader steps formation and during grounding (final jump phase - the very beginning of the return stroke), as well as during the formation of the subsequent return strokes.

Excitation of high-frequency electromagnetic waves in lightning and spark discharges is confirmed by the measurements [27, 28]. The surface plasmon waves can be interpreted as ionizing waves of the potential gradient [29]. Note that the propagation of fast ionization waves under electrical breakdown conditions were experimentally demonstrated in [30]. It was shown that the shorter the pulse front of the applied voltage and the stronger the pre-ionization of the discharge gap, the greater the speed of the ionization wave starting from the high-voltage electrode.

The measured speeds of the return stroke and illumination pulses are less than the speed of light [31, 32]. Optical measurements of return strokes speed are not available during the initial stages of natural lightning return strokes, but it can be evaluated from the measured electric fields and electric field derivatives. It was shown in [33] that the initial return stroke speed is actually near the speed of light  $c$  for the bottom 30 m of the triggered lightning channel. The current risetime increases with the height from the ground indicating that high frequency components propagate only for a short distance.

Note that the velocity values are usually underestimated due to the tortuosity of the breakdown channel. The real length of a tortuous and oblique channel is larger due to fractal nature of a lightning channel [34]. This implies that ultra-relativistic velocities for high-frequency surface plasmon waves in a lightning discharge channel are realistic. Calculations show that the velocities of the order of  $c/2$  correspond to the moderate values of the conductivity of the lightning channel.

### 3. Radiation of e/m waves

An electromagnetic wave in a plasma channel results in a time-dependent electric dipole (polarization) that generates a polarization current pulse propagating at a relativistic speed. It follows from the laws of electrodynamics that charged particles or dipoles moving with acceleration (or oscillation) should emit electromagnetic radiation. A polarization current pulse moving along a curved (circular) path generates a radiation similar to the synchrotron radiation produced by electrons circulating in a magnetic field.

There are numerous curvatures and irregularities on the tortuous lightning channel boundary (Fig. 3). The curvature of the trajectory introduces centripetal acceleration in the moving polarized region, thereby leading to electromagnetic radiation.

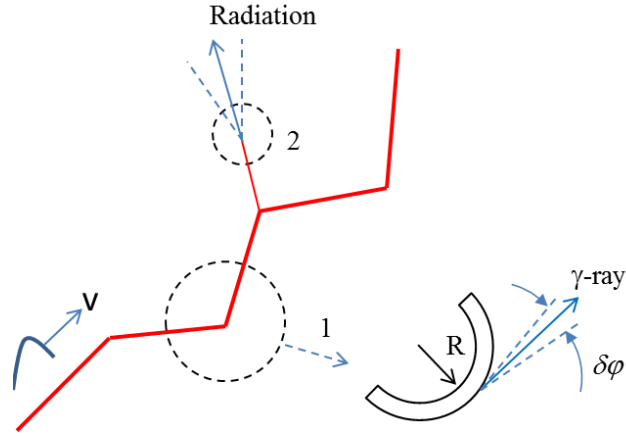


Fig. 3. Schematic view of a lightning channel. Sources (places) of radiation: 1 – synchrotron radiation; 2 – transition radiation.

The induced polarization defines the electric dipoles density, so the properties of the radiation are determined by the emission resulting from the motion of a dipole or from a charge  $e$  that moves with relativistic speed along a circular trajectory. The electromagnetic radiation generated by charges moving along a curved trajectory (synchrotron radiation) has been well known for a long time [35].

The power emitted into the  $m$ -th harmonic is given by [36, 37]:

$$W(m) = \frac{e^2 c m \alpha}{4\pi\epsilon_0 R^2} \left[ 2\alpha^2 J'_{2m}(2m\alpha) + (1-\alpha^2) \int_0^{2m\alpha} J_{2m}(x) dx \right], m = 1, 2, .. \quad (4)$$

where  $\alpha = v/c$ ,  $m$  is the harmonic order,  $R$  is the curvature radius of the trajectory bend.

In the non-relativistic case, the main contribution to the total power  $W = \sum_{m=1}^{\infty} W(m)$  gives the radiation of the first harmonic ( $m = 1$ , dipole radiation). The total radiation power of a non-relativistic electron is [37]:

$$W(1) = \frac{2}{3} \frac{e^2 c \alpha^4}{4\pi\epsilon_0 R^2}. \quad (5)$$

In the ultra-relativistic case, the total radiation power is given by [36, 37]:

$$W = \frac{2}{3} \frac{e^2 c}{4\pi\epsilon_0} \frac{\alpha^4 \gamma^4}{R^2}, \quad (6)$$

where  $\gamma = (1 - v^2/c^2)^{-1/2}$  is the relativistic Lorentz factor,  $\alpha = v/c$ ,  $e$  is the electron charge,  $v$  is the velocity of the surface plasmon wave (polarization density),  $c$  is the speed of light in vacuum, and  $R$  is the curvature radius of the trajectory bend.

Power spectrum is defined by [37]

$$\frac{dW}{dy} = WF(y), \quad (7)$$

where  $F(y) = \frac{9\sqrt{3}}{8\pi} y \int_y^\infty K_{5/3}(x) dx$ ,  $K_p(x)$  is the Macdonald function,  $y = \frac{\omega}{\omega_c}$ ,  $\omega_c = \omega_0 \gamma^3$ .

The spectral power density of the radiation in the low frequency region ( $y \ll 1$ ) is given by

$$\frac{dW}{d\omega} \approx \frac{e^2 \omega_c}{c \varepsilon_0 \gamma^2} \left( \frac{\omega}{\omega_c} \right)^{1/3}.$$

In the high-frequency region ( $y \gg 1$ ) the spectral power density has the form:

$$\frac{dW}{d\omega} \approx \frac{e^2 \omega_c}{c \varepsilon_0 \gamma^2} \left( \frac{\omega}{\omega_c} \right)^{1/2} \exp\left( -\frac{2}{3} \frac{\omega}{\omega_c} \right).$$

The maximum in the spectral power distribution is achieved at the frequency  $\omega_{\max} = \frac{1}{2} \gamma^3 \omega_0$ , where  $\omega_0 = v/R$ . [37]. The radiation is concentrated mainly in a narrow cone with an axis along the direction of the velocity. The angular width  $\Delta\theta$  in which the main part of the radiation is enclosed is inverse proportional to the relativistic Lorentz factor:  $\Delta\theta \sim 1/\gamma$ . This indicates that the ultra-relativistic velocities of the polarization bunch lead to a very narrow spatial distribution of X-rays and gamma rays.

Strong linear polarization of radiation occurs in the orbital plane. Moreover, the degree of polarization is equal to 3/4 [37]. Total powers of  $\sigma$ - and  $p$ - polarization components  $W_\sigma$  and  $W_\pi$ , are equal to  $W_\sigma = 7/8$  and  $W_\pi = 1/8$  [37]. In the plane of the orbit of revolution, the radiation is completely linearly polarized, since  $W_\pi = 0$ .

Note that polarization can serve as an accurate criterion for testing hypotheses about the nature of radiation. In particular, according to measurements of the polarization of electromagnetic radiation from the Crab Nebula, the synchrotron nature of radiation was established [38].

In Fig. 4 the spectral distribution of the radiation is presented. The spectral distribution has a maximum near  $\omega \approx \omega_c/3$ , where  $\omega_c = (3/2)\omega_0 \gamma^3$ , and the main part of the radiation is concentrated in this frequency range. These radiation frequencies are very large compared to the distance between two adjacent ones. The radiation spectrum consists of a very large number of closely spaced lines, i.e. it has a quasi-continuous character.



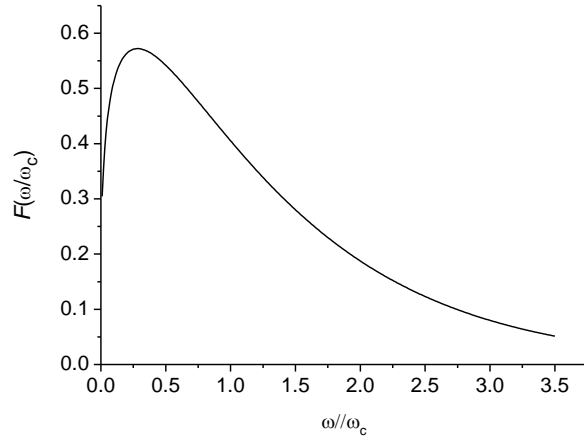


Fig. 4. Spectral distribution of the radiation.

In Fig. 5 the photon frequency as function of the conductivity are presented for different values of the surface wave frequency.

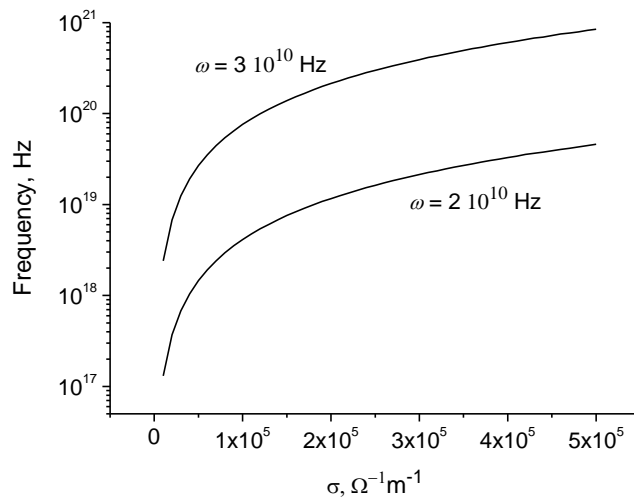


Fig. 5. Photon frequency as function of conductivity.  $r_0 = 0.01$  m.

In Fig. 6a the values  $\gamma = (1 - v^2/c^2)^{-1/2}$  as a function of the conductivity are presented. In Fig 6b the photon frequency as a function of the conductivity is shown.

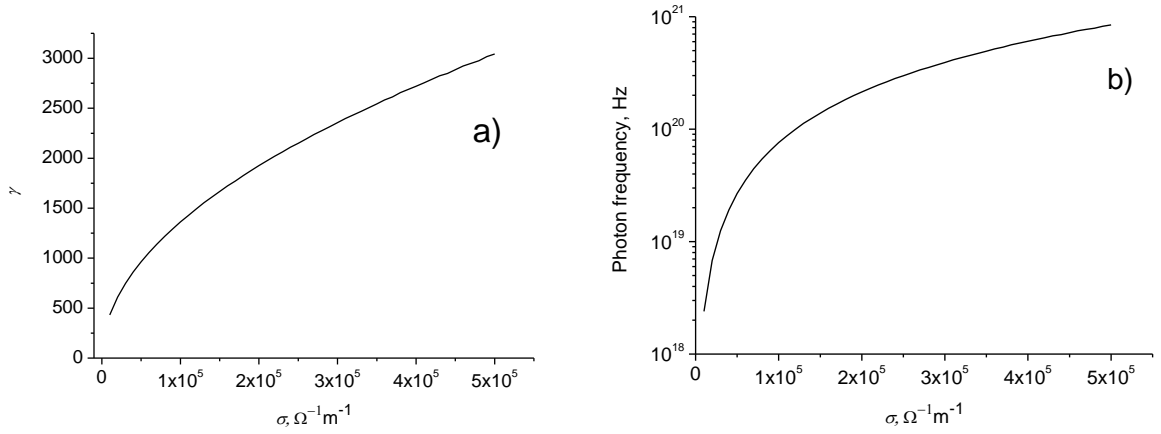


Fig. 6. The Lorentz factor as function of conductivity.  $\omega = 2\pi f = 3 \cdot 10^{10}$  Hz,  $r_0 = 0.01$  m.

In Table 1 the attenuation lengths, Lorentz factors, photon frequencies and energies are presented for different values of the channel conductivity and surface wave frequency.

Table 1. Relationships between lightning and X-ray and gamma-ray radiation parameters.

$$r_0 = 0.01 \text{ m}, f = \omega/2\pi.$$

$\sigma, \Omega^{-1}\text{m}^{-1}$	$f, \text{Hz}$	$z_0, \text{m}$	$\gamma$	$\omega_{ph}, \text{Hz}$	$E_{ph}, \text{eV}$
$10^4$	$10^8$	175	17	$1.48 \cdot 10^{14}$	0.1
	$10^9$	27.2	27.7	$0.64 \cdot 10^{15}$	0.42
	$5 \cdot 10^9$	4.2	441	$2.57 \cdot 10^{18}$	1690
$10^5$	$10^8$	556	31.7	$0.96 \cdot 10^{15}$	0.63
	$10^9$	85.5	52.8	$4.4 \cdot 10^{15}$	2.9
	$5 \cdot 10^9$	13.3	1393	$8.1 \cdot 10^{19}$	53350
$10^6$	$10^8$	1667	59	$6.16 \cdot 10^{15}$	4.05
	$10^9$	267	100	$3 \cdot 10^{16}$	19.7
	$5 \cdot 10^9$	42	4389	$2.54 \cdot 10^{21}$	1670000

Thus, the spectrum of synchrotron radiation of lightning covers almost the entire scale of electromagnetic waves - from the radio frequency to the X-rays and gamma rays.

In Fig 7 the photon frequency and energy as a function of the conductivity are shown.

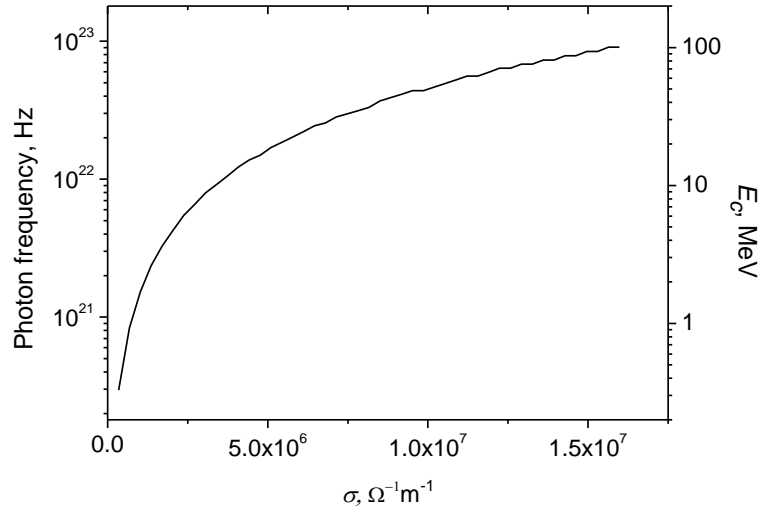


Fig. 7. The photon frequency and energy as function of conductivity.  $\omega = 2\pi f = 3.1 \cdot 10^{10}$  Hz,  $r_0 = 0.01$  m.

In Fig. 8 the calculated and measured photon counts per energy band  $dE_{ph}$  are presented.

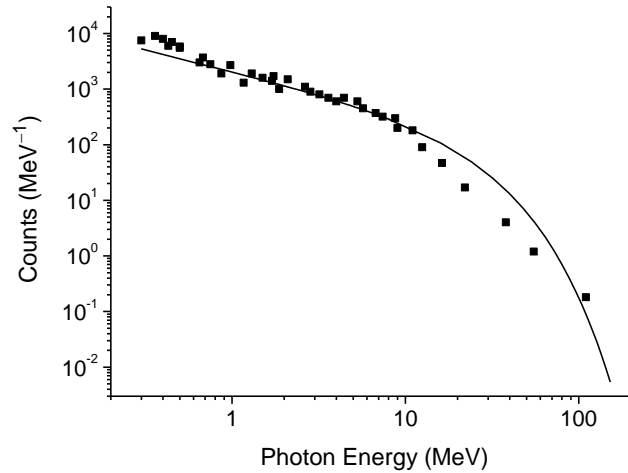


Fig. 9. The normalized photon spectrum (solid curve) and measured spectrum from AGILE [13].  $E_c = 16$  MeV

It is seen that there is not exponential cutoff near 10 MeV in contrast to RREA models.

Our model is also consistent with the measured spectrum from laboratory spark discharge [7]. In Fig. 9 the calculated and measured photon counts from laboratory spark discharge are presented. A power-law spectrum is seen for energies less than 1 MeV, while the exponential decrease is observed at high energies.

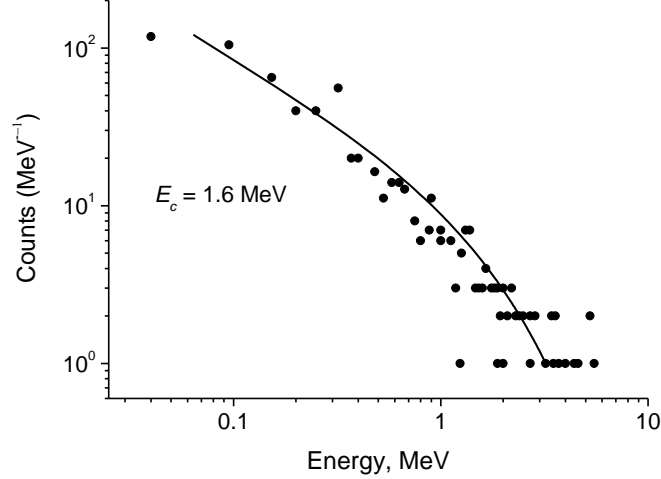


Fig. 9. The normalized photon spectrum (solid line) and measured spectrum from laboratory spark discharge [7].  $E_c = 1.6$  MeV.

#### 4. Photon number

The number of photons with frequencies  $\omega_{\max} \approx \omega_0 \gamma^3$  radiated for the time  $\delta t \approx 1/\omega_0$  of the electron's revolution around the circle is given by

$$N_{ph} \sim \frac{W}{\omega_0 \hbar \omega_{\max}} \sim \frac{e^2}{\hbar c \epsilon_0} \gamma \approx \frac{2.56 \cdot 10^{-38} \gamma}{1.05 \cdot 10^{-34} \cdot 3 \cdot 10^8 \cdot 8.85 \cdot 10^{-12}} \approx 10^{-1} \gamma. \quad (8)$$

This number of photons corresponds to the radiation over time  $\delta t \sim 10^{-10}$  s. For a time of 1  $\mu$ s, the number of photons is equal to  $N_{ph} \sim 10^3 \gamma$ .

For single charges, the radiation is weak. The situation changes when we consider bunches of particles. Indeed, the polarization of the plasma occurs in a certain extended region, so as a result, the amplitude of the polarization radiation will be determined by the total dipole moment of the bunch. In this case, a bunch of polarized plasma will radiate like point particles with a charge and multipole moments corresponding to the entire bunch.

The power of synchrotron radiation consists of coherent and incoherent parts [37]:

$$W(m) = W^{incoh}(m) + W^{coh}(m).$$

When radiation is incoherent, the total power is given by [37]:

$$W_N(m) = N_e \cdot W(m),$$

where  $N_e$  is the number of electrons in a polarized plasma bunch.

Number of electrons in a polarized plasma bunch is determined by the polarization current  $i_{pol}$  :

$$N_e \approx \frac{Q}{e} \approx \frac{i_{pol} \cdot \Delta t}{e},$$

where  $\Delta t \sim \tau_f \sim 1/\omega \sim 10^{-10}$  s.

The current density in Maxwell equation for the electric field acquires an additional term:

$$\vec{j} = \sigma \vec{E} + \frac{\partial \vec{P}}{\partial t} = \sigma \vec{E} + \varepsilon_0 (\varepsilon - 1) \frac{\partial \vec{E}}{\partial t}, \quad (9)$$

where  $\vec{j}_{cond} = \sigma \vec{E}$  is the conduction current and  $\vec{j}_{pol} = \frac{\partial \vec{P}}{\partial t}$  is the polarization current.

The ratio of the amplitudes of conduction and polarization currents is determined by

$$\frac{j_{cond}}{j_{pol}} = \frac{\sigma}{\omega \varepsilon_0 |\varepsilon - 1|} = \frac{\nu}{\omega}, \quad (10)$$

where  $\nu$  is the collision frequency,  $\omega$  is the frequency of the surface wave field,

$\sigma = \omega \varepsilon_0 \varepsilon'' = \frac{n_e e^2 \nu}{m(\omega^2 + \nu^2)}$ ,  $\varepsilon' = 1 - \frac{\omega_p^2}{\omega^2 + \nu^2}$ ,  $\varepsilon'' = \frac{\sigma}{\omega \varepsilon_0} \gg |\varepsilon'|$ ,  $\omega_p^2 = \frac{4\pi n_e e^2}{m}$  is the plasma or Langmuir frequency of electron gas oscillations.

It follows from (5) that the polarization current is two orders of magnitude less than the conduction current. If the conduction current is on the order of 100 kA, then the polarization current will be on the order of 1 kA.

For the number of electrons we obtain

$$N_e \approx \frac{Q}{e} \approx \frac{i_{pol} \cdot \Delta t}{e} \sim \frac{10^3 \cdot 10^{-9}}{1.6 \cdot 10^{-19}} \sim 10^{12+13}.$$

Thus, for the number of photons radiated for a time of 1  $\mu$ s we have:

$$N_{ph} \approx 10^3 \gamma \cdot N_e \approx 10^3 \cdot 10^3 \cdot 10^{12+13} \sim 10^{18+19} \text{ photons.}$$

This estimated photon number is in the range of observation data. Note that the typical brightness of a TGF observed from space is within an order of magnitude of  $10^{17} - 10^{19}$  gamma rays [9, 39].

The radiation power increases dramatically in the case of coherent bunch of electrons grouped at distances less than the wavelength of the emitted wave. The coherent radiation can be observed in low-frequency range, i.e., in the radio-frequency one. It is known that the radio-frequency pulses of pulsars are emitted by a coherent synchrotron mechanism [40]. The radiation power increases

dramatically in the case of coherent bunch of electrons grouped at the distances less than the wavelength of the emitted wave. In this case the radiation power is given by  $W^{tot} = N_e^2 \cdot W$ .

High-intensity microwave radiation of a lightning discharge was observed in [27, 41-43]. The extreme brightness of the radiation observed from fast radio bursts indicates that it is generated in the process of coherent radiation. It was shown in [41] that the microwave radiation from lightning is a sequence of individual pulses, and the radiation spectrum differs from the spectrum in the long-wave range. This indicates that in the decimeter range, the mechanism of generating electromagnetic waves differs from the usual dipole radiation of the lightning current. Recently it was shown that each leader step emits a burst of multiple discrete vhf pulses [15].

### *Transition radiation*

Another mechanism for producing microwave, X-ray and gamma-ray during the propagation of a surface wave along the discharge channel is the transition radiation [44]. Transition radiation occurs when polarization distribution (electric dipoles) moves at a speed exceeding the phase speed of light in the medium. However, the power of transition radiation is much lower than that of synchrotron radiation. The power increases greatly with coherent transient radiation.

The total energy radiated by an electron is given by [44]:

$$P = \frac{e^2 \omega_p}{3c \epsilon_0} \gamma, \quad \omega_p^2 = \frac{ne^2}{m \epsilon_0}.$$

The number of photons is determined by

$$N_{ph} = \frac{P}{\hbar \omega_{ph}} = \frac{e^2 \omega_p}{3c \epsilon_0 \hbar \omega_{ph}} \gamma.$$

This number is much smaller than that of synchrotron radiation. However, the number of photons increases significantly with coherent transient radiation, i.e. for the radio frequency range.

## **5. Discussion**

It follows from the simulation that the conductivity and radius of the discharge channel are the main critical parameters to initiate the X-ray and gamma-ray emissions. High conductivity can be created by the return stroke current, so the gamma-ray emission is produced by the pulses moving along a channel after the start of the return stroke. It was shown in [4] that the gamma-ray flashes with the highest energy exceeding 20 MeV occurred well after the start of the return stroke. This is consistent with our result that the gamma-ray flash with harder energy spectrum is associated with the higher conductivity and larger radius of a lightning channel. TGF flashes from the leader steps should have softer energy spectrum because of the lower conductivity and smaller radius of a leader channel.

It was shown recently, that TGFs are produced during strong initial breakdown pulses (IBPs) in the beginning stages of negative-polarity breakdown [45, 46]. Similar effect was shown in [47], where X-rays were only observed during the leader before the return stroke with the highest peak current.

Depending on the conductivity and radius of a discharge channel, the energy spectrum of the radiation extends from the radio-frequency to X-ray and gamma-ray. This indicates that the same source regions are responsible for these radiations. Indeed, the correlation of X-ray emission with radio wave radiation is recorded in measurements in [15, 48].

Recently radio-frequency radiation (30-80 MHz) which correlates with the X-ray and gamma-ray radiations was observed at each step of a negative lightning leader [15]. It was shown that the vhf emission is concentrated near the tip of the leader, as well as along the body of the step.

We assume that high intensity radio-frequency pulses from a lightning discharge are emitted by a coherent mechanism, and X-rays and gamma rays can be interpreted using the mechanism of incoherent synchrotron radiation.

In contrast to TGF models based on the RREA process [4, 9-12], which produce a typical electron energy spectrum close to exponential, our model gives a long tails in the photon power spectrum.

It follows from our model that the X-ray and gamma-ray radiations are concentrated in a narrow cone. Spatial location of the source region within discharge channel and the radiation pattern (orientation) depend also on the tortuosity and branches of the channel. This will cause the strong dependence of the detected radiation power on the direction of the detector. It was shown in [47] that the orientation of the descending leader plays an important role in the detection of X-rays. It was also pointed out in [7], that the x-ray bursts in a laboratory spark discharge have a finite opening cone.

Note that the proposed synchrotron radiation mechanism, unlike the existing models, does not require a large-scale region of a high-intensity electric field to accelerate the electrons and seed particles necessary for the RREA processes.

## **Conclusions**

To conclude, the theoretical model of X-ray and gamma-ray emissions, as well as radio-frequency radiation produced by Lightning discharge via synchrotron and transition radiation mechanisms is consistent with the observational data. The proposed model is characterized by a wide spectral range on the scale of electromagnetic waves and acute collimation, which provides high source brightness, high power, and strong linear polarization of the radiation. The source of synchrotron radiation of lightning is the polarization density distribution (the pulse of the polarization current) and associated surface electromagnetic wave, moving along a curved and irregular ionized channel with a relativistic velocity. The existence of long tails in the power spectrum is shown, which explains observations of photon energies in the range of 10-100 MeV in the TGF. Polarization can serve as an accurate criterion for testing hypotheses about the synchrotron nature of lightning high-energy radiation. Therefore, observations of the polarization and beaming properties are necessary to confirm the synchrotron nature of the X-ray and gamma-ray radiation produced by a lightning discharge.

## References:

1. C. T. R. Wilson, Proc. Cambridge Phil. Soc. **22**, 534 (1925).
2. T. Enoto, Y. Wada, Y. Furuta, *et al.*, Nature **551**, 481 (2017).
3. G. J. Fishman, P. N Bhat, R. Mallozzi, J. M. Horack, T. Koshut, C. Kouveliotou, G. N. Pendleton, C. A. Meegan, R. B. Wilson, W. S. Paciesas *et al.*, Science **264**, 1313 (1994).
4. J. R. Dwyer, M.M. Schaal, E. Cramer, S. Arabshahi, N. Liu, H. K. Rassoul, J.D. Hill, D.M. Jordan, and M.A. Uman, J. Geophys. Res. **117**, A10303 (2012).
5. Y. Wada, T. Enoto, K. Nakazawa, Y. Furuta, T. Yuasa, Y. Nakamura, T. Morimoto, T. Matsumoto, K. Makishima, and H. Tsuchiya, Phys. Rev. Lett. **123**, 061103 (2019).
6. M.M. Schaal, J. R. Dwyer, Z. H. Saleh, H. K. Rassoul, J. D. Hill, D. M. Jordan, and M. A. Uman, J. Geophys. Res. **117**, D15201 (2012).
7. P.O. Kochkin, A.P. J. van Deursen and U. Ebert, J. Phys. D: Appl. Phys. **48**, 025205 (2015).
8. A.V. Gurevich, G.M. Milikh, and R. Roussel-Dupre, Phys. Lett. A **165**, 463 (1992).
9. J. R. Dwyer and D. M. Smith, Geophys. Res. Lett. **32**, L22804 (2005).
10. J. R. Dwyer, M. A. Uman, Phys. Rep. **534**, 147 (2014).
11. W. Xu, S. Celestin, V.P. Pasko, Geophys. Res. Lett. **41**, 7406 (2014).
12. L.P. Babich, E.I. Bochkov, I.M. Kutsyk, T. Neubert, and O. Chanrion, J. Geophys. Res.: Space Physics **120**, 5087 (2015).
13. M. Tavani, M. Marisaldi, C. Labanti, F. Fuschino, A. Argan, A. Trois, P. Giommi, S. Colafrancesco, C. Pittori, F. Palma, and *et al.*, Phys. Rev. Lett. **106**, 018501 (2011).
14. D. J. Pleshinger, S.T. Alnussirat, J. Arias, S. Bai, Y. Banadaki, M.L. Cherry, *et al.*, J. Geophys. Res.: Space Physics **124**, 9229 (2019).
15. B. M. Hare, O. Scholten, J. Dwyer, U. Ebert, *et.al.*, Phys. Rev. Lett. **124** , 105101 (2020).
16. T. Neubert, N. Østgaard, V. Reglero, O. Chanrion, M. Heumesser, K. Dimitriadou, F. Christiansen, C. Budtz-Jørgensen, I. Kuvvetli, I. L. Rasmussen, *et.al.*, Science **367**, 183 (2020).
17. N. Ostgaard, T. Neubert, V. Reglero, K. Ullaland, S. Yang, G. Genov, *et al.*, J. Geophys. Res.: Atmospheres **124**, 14024 (2019).
18. S.T. Alnussirat, H. J. Christian, G. J. Fishman, J. Burchfield, M. L. Cherry, Phys. Rev. D **100**, 083018 (2019).



19. M. Heumesser, O. Chanrion, T. Neubert, H.J. Christian, K. Dimitriadou, F.J. Gordillo-Vazquez, *et. al.*, *Geophys. Res. Lett.* **48**, e2020GL090700 (2021).
20. A. Sommerfeld, *Ann. Phys. Chem.* **67**, 233 (1899).
21. N. I. Petrov, *Sci. Rep.* **9**, 18332 (2019).
22. M.A. Uman, *J. Geophys. Res.* **69**, 583 (1964).
23. R.E. Orville, J.H. Helsdon Jr., W.H. Evans. *J. Geophys. Res.* **79**, 4059 (1974).
24. J. Cen, Q. Hou, P. Yuan, *et.al.*, *AIP Advances* **8**, 085019 (2018).
25. J. Cen, P. Yuan, S. Xue, X. Wang, *Appl. Phys. Lett.* **106**, 054104 (2015).
26. N.I. Petrov and R.T. Waters, *Proc. Roy. Soc. A* **450**, 589 (1995).
27. E.P. Krider, C. Leteinturier, J.C. Willet, *J. Geophys. Res.* **101**, 1589 (1996).
28. N.I. Petrov, V.R. Avanskii, and N.V. Bombenkova, *Tech. Phys.* **39**, 546 (1994).
29. L.B. Loeb, *Science* **148**, 1417 (1965).
30. L.M. Vasilyak, S.V. Kostyuchenko, N.N. Kudryavtsev, I.V. Filyugin, *Phys. Usp.* **37**, 247 (1994).
31. C. Liang, B. Carlson, N. Lehtinen, M. Cohen, R. A. Marshall, and U. Inan. *Geophys. Res. Lett.* **41**, 2561 (2014).
32. F.L. Carvalho, D.M. Jordan, M.A. Uman, T. Ngin, W.R. Gameraota, and J.T. Pilkey, *Geophys. Res. Lett.*, **41**, 7799 (2014).
33. R. Thottappillil, J. Schoene and M.A. Uman, *Geophys Res. Lett.* **28**, 3593 (2001)
34. N. I. Petrov and G. N. Petrova, *Tech. Phys.* **38**, 287 (1993); *Tech. Phys.* **44**, 472 (1999); N. I. Petrov, G. N. Petrova, and F. D'Alessandro, *IEEE Trans. on Diel. Electr. Insul.* **10**, 641 (2003).
35. G.A. Schott, *Ann. der Phys.* **24**, 635 (1907); *Electromagnetic Radiation* (Cambridge, 1912).
36. A.A. Sokolov and I.M. Ternov. *Sov. Phys. JETP* **4**, 396 (1957).
37. I.M. Ternov, *Phys. Usp.* **38**, 409 (1995).
38. V.L. Ginzburg and S.I. Syrovatskii. *Sov. Phys. Usp.* **8**, 674 (1966).
39. B.G. Mailyan, M. S. Briggs, E. S. Cramer, G. Fitzpatrick, O. J. Roberts, M. Stanbro, V. Connaughton, S. McBreen, P. N. Bhat, and J. R. Dwyer, *J. Geophys. Res. Space Physics* **121**, 11,346 (2016).
40. F.C. Michel, *Phys. Rev. Lett.* **48**, 580 (1982).
41. E.L. Kosarev, V.G. Zatsepin, and A.V. Mitrofanov, *J. Geophys. Res.* **75**, 7524 (1970).

42. V.F. Fedorov, Y.A. Frolov, and P.O. Shishkov, *J. Appl. Mech. and Tech. Phys.* **42**, 392 (2001).
43. D. Petersen and W. Beasley, *Atmos. Res.* **135-136**, 314 (2014).
44. V. L. Ginzburg, *Phys. Usp.* **39**, 973 (1996).
45. F. Lyu, S. A. Cummer, and L. McTague, *Geophys. Res. Lett.* **42**, 6836 (2015).
46. J.W. Belz, P.R. Krehbiel, J. Remington, M.A. Stanley, R.U. Abbasi, R. LeVon, W. Rison, D. Rodeheffer, T. Abu-Zayyad, M. Allen, *et al.*, *J. Geophys. Res.: Atmospheres*, **125**, e2019JD031940 (2020).
47. M. M. F. Saba, M. A. S. Ferro, E. T. Cuadros, D. M. Custódio, A. Nag, C. Schumann, V. Cooray, A. R. Paiva, P. B. Lauria, D. S. F. Medeiros, *et al.*, *J. Geophys. Res.: Space Physics*, **124**, 10564 (2019).
48. B. G. Mailyan, A. Nag, J. R. Dwyer, R. K. Sais, M. S. Briggs, O. J. Roberts, M. Stanbro, and H. K. Rassoul, *Sci. Rep.* **10**, 7286 (2020).